Dynamically Reconfigurable Force-Balanced Aerial Manipulator for Varying Payload Tasks

Bianconi, Michele; Brummelhuis, Martijn; Hamaza, Salua

DOI
10.1109/AIM64088.2025.11175741

Publication date
2025

Document Version
Final published version

Published in
2025 IEEE/ASME International Conference on Advanced Intelligent Mechatronics, AIM 2025

2025 IEEE/ASME International Conference on Advanced Intelligent Mechatronics (AIM) | 979-8-3315-3342-7/25/$31.00 ©2025 IEEE | DOI: 10.1109/AIM64088.2025.11175741

Dynamically Reconfigurable Force-Balanced Aerial Manipulator for Varying Payload Tasks

Michele Bianconi, Martijn Brummelhuis, Salua Hamaza

***Abstract*—This research proposes a novel, dynamically reconfigurable, and force-balanced aerial manipulator design for fast variable payload tasks. Its force-balancing minimizes aerial platform disturbances from the manipulator during fast end-effector movements. The manipulator is composed of three pantograph legs connecting the end-effector to the drone base, each equipped with two countermasses moved by bespoke fast linear actuators that ensure force-balancing of the manipulator for different payloads. Testing on a floating base setup and in flight showed a 45% reduction in reaction forces transferred to the base in the balanced vs. unbalanced configurations with no payload, and 17% with a 53 g payload. The position-tracking error in flight reduced with 19% and 34%, respectively.**

***Index Terms*—Aerial Manipulation, Force-Balanced Mechanisms, Mechanism Design, Parallel Aerial Manipulator.**

I. Introduction

Aerial manipulation, which combines robotic manipulators with aerial platforms like multicopters, has garnered extensive attention for its ability to extend the workspace almost indefinitely, constrained primarily by the drone's flight time. Applications include sensor placement [1], contact inspection [2], aerial repair [3], construction [4], and load delivery [5].

Despite progress, challenges remain in controlling the coupled dynamics between the manipulator and aerial platform. Reaction forces and moments generated by manipulator movements can destabilize the platform. Centralized control approaches [6] model the system as a single entity to account for coupling, but yields complex dynamic models. Fully-actuated platforms [7] mitigate disturbances but increase system complexity. Decentralized control, treating manipulator reactions as external disturbances, simplifies development but requires lightweight manipulators to keep reaction forces manageable [8]. This approach struggles with high-speed manipulator movements, which can lead to platform instability.

An alternative solution involves improving manipulator design to decouple dynamics. Prior work has explored balancing techniques to limit coupling effects. For example, Hamaza *et al.* used a countermass on a four-bar linkage to mitigate moment arms [9]. Various balancing strategies — dynamic-, force-, and static balancing — have been proposed to reduce reaction forces and moments. Theoretical advancements include the force-balancing conditions for Clavel's Delta robot [10], dynamically balanced multi-degree-of-freedom mechanisms using balanced parallel-piped designs [11], and families of force-balanced parallel manipulators [12]. Notable implementations include a dual-arm aerial manipulator with center-of-gravity (COG) balancing [13], a serial manipulator with a moving counter-mass [14], and a balanced pantograph gripper for aerial pick-and-place tasks [15].

The authors are with the Biomorphic Intelligence Lab, Department of Control & Operations, Faculty of Aerospace Engineering, TU Delft.

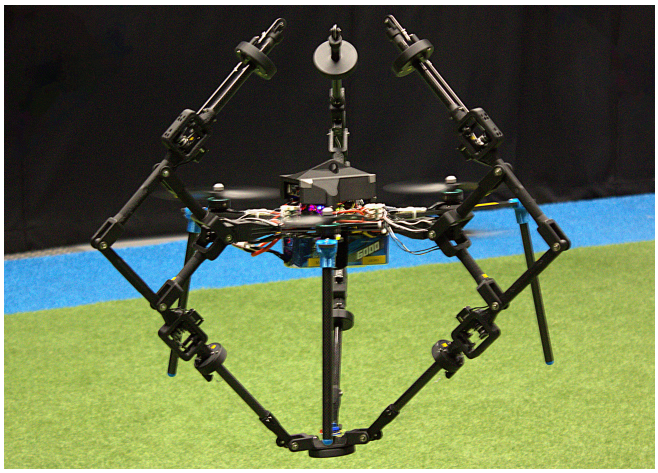

Fig. 1: Reconfigurable force-balanced aerial manipulator in flight.

Although theoretical advancements have been shown, practical implementations remain limited. Kartik *et al.* developed a force-balanced parallel manipulator for drones, but its fixed payload configuration limits its usability for varying payload tasks [16]. Similarly, Clark *et al.* presented a balanced delta-like manipulator, yet design integration challenges restricted its impact on platform performance [17].

A research gap in existing balanced designs is their inability to adapt to variable payloads, which is essential for interaction tasks like pick-and-place operations. De Jong *et al.* proposed reconfiguration strategies for balancing under varying payloads, including counter-mass positioning, joint location adjustments, and weight modifications [18]. To address these limitations, we propose a force-balanced, reconfigurable aerial manipulator capable of adapting to variable payloads (shown in flight in Figure 1). The primary contributions of this work are:

- Development of a novel reconfigurable force-balanced manipulator with lightweight, fast linear actuators for counter-mass movement;
- A novel aerial platform design with morphology optimized to integrate the manipulator;
- Comprehensive experimental validation of system's performance in both fixed-rig and flight tests.

II. Force-balanced Aerial Manipulator

Force-balanced manipulators advance aerial systems by minimizing reaction forces from movement on the drone base, which specifically benefits quadrotors unable to counteract such disturbances directly. The following section describes the design, fabrication, and control of a reconfigurable, force-balanced aerial manipulator for variable payload tasks.

A. Kinematics

The manipulator morphology [16] consists of a fixed base and a moving platform end-effector. Three parallel kinematic chains connect the two, forming a 3 degree of freedom (DOF) parallel manipulator. Each leg is a pantograph, of which only the lower portion defines the kinematics.

Figure 2 shows the kinematic parameters of the lower portion of a single pantograph. The center of the fixed base (manipulator base frame) is represented by O. E represents the center of the moving base (the end-effector). The Cartesian coordinate frame is defined at the origin O. For each pantograph, a coordinate system $x_{0i}y_{0i}z_{0i}$ is defined where $i = 1, 2, 3$ is the pantograph leg number. These coordinate systems share the same xy-plane but are rotated by angle θ_i such that x_{0i} points towards the attachment point of pantograph i. The radii of the base and end-effector are denoted by r_A and r_B. The joint angles are denoted by ϕ_{ji}, with $j = 1, 2, 3$ the joint number from the base. To solve the forward kinematics, the transformation matrix from point O to point E is derived using the Denavit-Hartenberg convention.

Unlike other parallel manipulators [19, 20] since the active joint comes after a passive joint the inverse kinematics cannot be solved analytically [16]. Hence, to find a solution for the end-effector position with respect to the active joints geometrical reductions are necessary. First, note that the length of vector OE is not dependent on ϕ_{3i}, therefore, by squaring and adding the expression for the end-effector position, we obtain an equation for the passive joint ϕ_{2i} as a function of ϕ_{1i}. By substituting this equation into the equation for z_E we obtain a relation between the passive joint ϕ_{3i} and the active joint ϕ_{1i}. Finally, by replacing the relations between the passive joints and the active joint in the original set of equations for end-effector position, an relation between the desired end-effector positions and the active joint ϕ_{1i} is found.

As the relation is highly non-linear, numerical solvers struggle to find the correct solution despite various initial conditions, requiring a different approach. From a starting solution space of ϕ_{1i} angles, the passive joints are iteratively solved from the relations previously described. Since $\phi_{3i} = \arccos f(\phi_{1i}, x_E, y_E, z_E)$ for each ϕ_{1i}, two solution sets exist:(ϕ_{1i},ϕ_{2i},ϕ_{3i}) and (ϕ_{1i},ϕ_{2i},$-\phi_{3i}$). The joint limits are verified and the end-effector position is computed. If the computed position corresponds to the desired end-effector position, the solution is found.

B. Workspace analysis

To determine the manipulator dimensions, a sensitivity analysis of the workspace was performed by varying r_A, r_B, L_1, and L_2. The workspace outline was obtained by solving inverse kinematics iteratively in the positive xz-quadrant and revolving the outline around the z-axis.

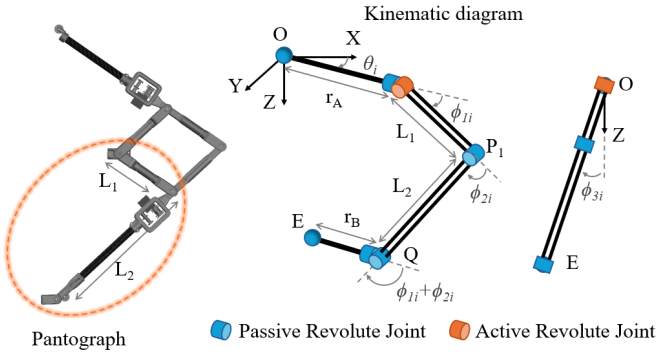

Fig. 2: Schematic diagram of the lower portion of one of the pantograph legs which make up the parallel manipulator. Geometric definitions for the links and joints in the diagram are used to formulate the kinematic model of the manipulator.

An efficient search algorithm finds the outline. First, vertical bounds are determined by solving inverse kinematics near the z-axis. The algorithm then searches out and down, along the x- and z-axes until no solution is found (out of workspace).

Two metrics are introduced for workspace comparison: (1) maximum area of a rectangle within the workspace, indicating overall size, and (2) maximum width of a 10 mm-high rectangle, emphasizing width over height to prioritize lateral reach, as vertical adjustments are easily done by the aerial platform.

The initial configuration uses $r_A = 160$ mm, $r_B = 140$ mm, $L_1 = 220$ mm, and $L_2 = 250$ mm. The search space is defined for r_A and r_B between 0.5–1.5x the initial value and for L_1, L_2 between 0.5–2.0x the initial value. Results are shown in Figure 3A.

This figure shows that increasing r_A beyond 180 mm or decreasing r_B below 120 mm provides no additional benefit. Increasing L_1 and L_2 improves both metrics, with the maximum area benefiting more than the maximum width. Based on this analysis, r_A and r_B were set to 180 mm and 65 mm, respectively. The r_A was maximized to fit the drone's electronics, while r_B was minimized to reduce weight and enhance the pantograph design's force balancing properties (subsection II-C). The dimensions of L_1 and L_2 will be determined in the next section.

C. Force-balancing optimization

Our manipulator configuration achieves force-balancing by combining 2D planar force-balanced elements into a 3D mechanism. The planar force-balanced elements (the pantographs), make up the three legs of the manipulator. Ensuring each pantograph is force-balanced then results in a force-balanced manipulator. The force balancing conditions of the pantograph mechanism, formulated by Van der Wijk [21], are reported below. Figure 3B shows the pantograph dimensions.

$$\begin{aligned} m_1 p_1 &= m_2 a_1 + m_3 p_3 \\ m_1 q_1 &= m_3 q_3 \\ m_2 p_2 &= m_1 a_2 + m_4 p_4 \\ m_2 q_2 &= m_4 q_4 \end{aligned} \tag{1}$$

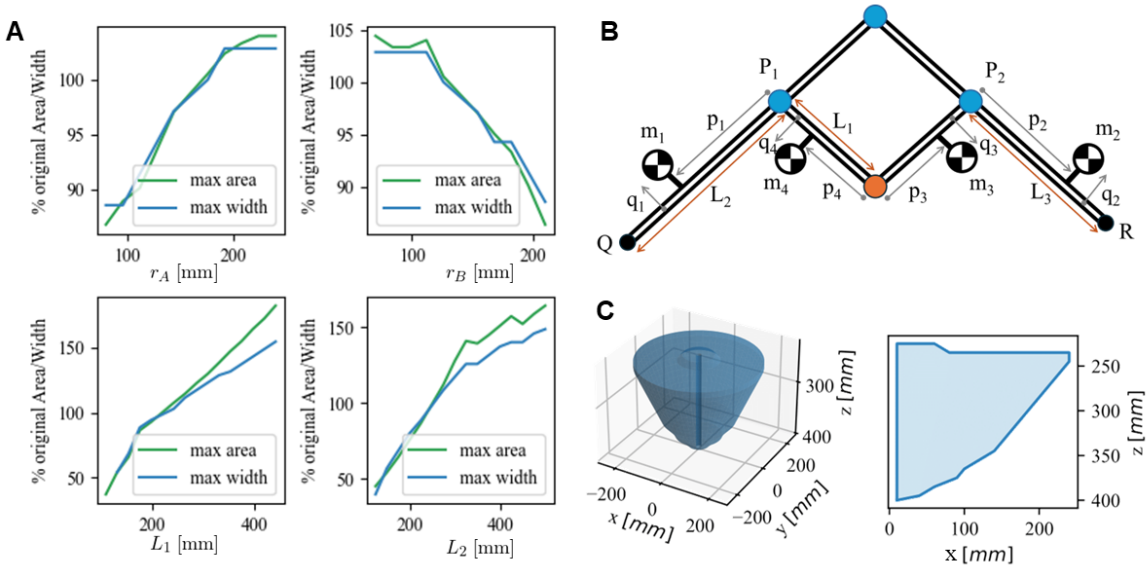

Fig. 3: A) Sensitivity analysis results show the effect of varying r_A, r_B, L_1, and L_2 on the workspace metrics. The maximum area represents the largest rectangle fitting within the workspace outline, while the maximum width represents the widest rectangle of 10 mm height fitting within the outline. Both increase with r_A, L_1, and L_2, but decrease with r_B. B) Schematic diagram defining the mass properties of the force-balanced pantograph mechanism. C) 3D workspace plot (left) and workspace outline (right) of the final manipulator design.

Where m_i indicates the mass of the respective link including counter mass. From the pantograph design, we assume that the center of mass (COM) of the links lies along their axes, leading to $q_1, q_2, q_3, q_4 = 0$. This reduces the system of equations to:

$$\begin{aligned} m_1 p_1 &= m_2 a_1 + m_3 p_3, \\ m_2 p_2 &= m_1 a_2 + m_4 p_4. \end{aligned} \tag{2}$$

For the manipulator to be force-balanced, the mass value m_1 includes the end-effector's mass, with each pantograph accounting for one-third of the weight in the m_1 term. This is balanced by introducing a countermass (CM) on the opposite side of the pantograph. Given fixed dimensions for p_1 and p_2, the pantograph is balanced only for only one manipulator configuration. If the end-effector mass changes, for example during a pick-and-place task or end-effector replacement, the manipulator would not remain force-balanced. To address this, moving countermasses are added to the P_1Q and P_2R links.

The $m_1 p_1$ and $m_2 p_2$ terms can be split in $\hat{m}_i \hat{p}_i$ and $m_{i\text{CM}} p_{i\text{CM}}$ for $i = 1, 2$, where $m_i p_i = \hat{m}_i \hat{p}_i + m_{i\text{CM}} p_{i\text{CM}}$. The first term represents the mass and COM position of all fixed components of link i, and the second term corresponds to the mass and COM position of countermass i. Furthermore, m_2 can be split such that $m_2 = \hat{m}_2 + m_\text{p}$, where $\hat{m}_2$ is one-third of the end-effector mass and m_p is the payload mass (i.e. the mass change). The payload mass location p_p is assumed to be equal to the link length L_2. To find the relation between countermass locations $p_{1\text{CM}}$, $p_{2\text{CM}}$, and the payload mass m_p, the force-balancing equations can be rewritten to

$$\begin{aligned} p_{1\text{CM}} &= -\frac{p_\text{p} m_\text{p}}{3 m_{1\text{CM}}} + \frac{m_2 a_1 + m_3 p_3 - \hat{m}_1 \hat{p}_1}{m_{1\text{CM}}}, \\ p_{2\text{CM}} &= \frac{a_2 m_\text{p}}{3 m_{2\text{CM}}} + \frac{(\hat{m}_1 + m_{1\text{CM}})\, a_2 + m_4 p_4 - \hat{m}_2 \hat{p}_2}{m_{2\text{CM}}}. \end{aligned} \tag{3}$$

To determine the required mass of the countermasses, an iterative search ensures the pantograph remains force-balanced for both a minimum payload of 0 g (no payload) and a maximum payload of 60 g. A 60 g payload, increasing the end-effector mass by 66%, was selected to provide measurable effects during testing. Based on these payload limits, the required countermass positions $p_{1\text{CM}}$ and $p_{2\text{CM}}$ were calculated. The lightest combination of $m_{1\text{CM}}$ and $m_{2\text{CM}}$ satisfying the pantograph's geometric constraints is chosen as the solution.

To determine link dimensions L_1 and L_2, an smart search algorithm on the force balancing relations was performed. These links correspond to the dimensions $a_1 = a_2$ and member P_1Q in Figure 3B. Mass and COM positions of all joint components were determined from an original pantograph prototype. Masses for links with dimensions a_1, a_2, P_1Q, and P_2R were expressed as functions of their dimension. From this, the pantograph's force-balanced configuration can be determined as a function of L_1, L_2, L_3 (corresponding to link P_2R), and m_E (corresponding to the end-effector structure mass). The total manipulator mass including joints, links and countermasses, was minimized. The search variables were constrained as follows: L_1 and L_3 between 100 mm and 160 mm, L_2 between 280 mm and 330 mm, and m_E between

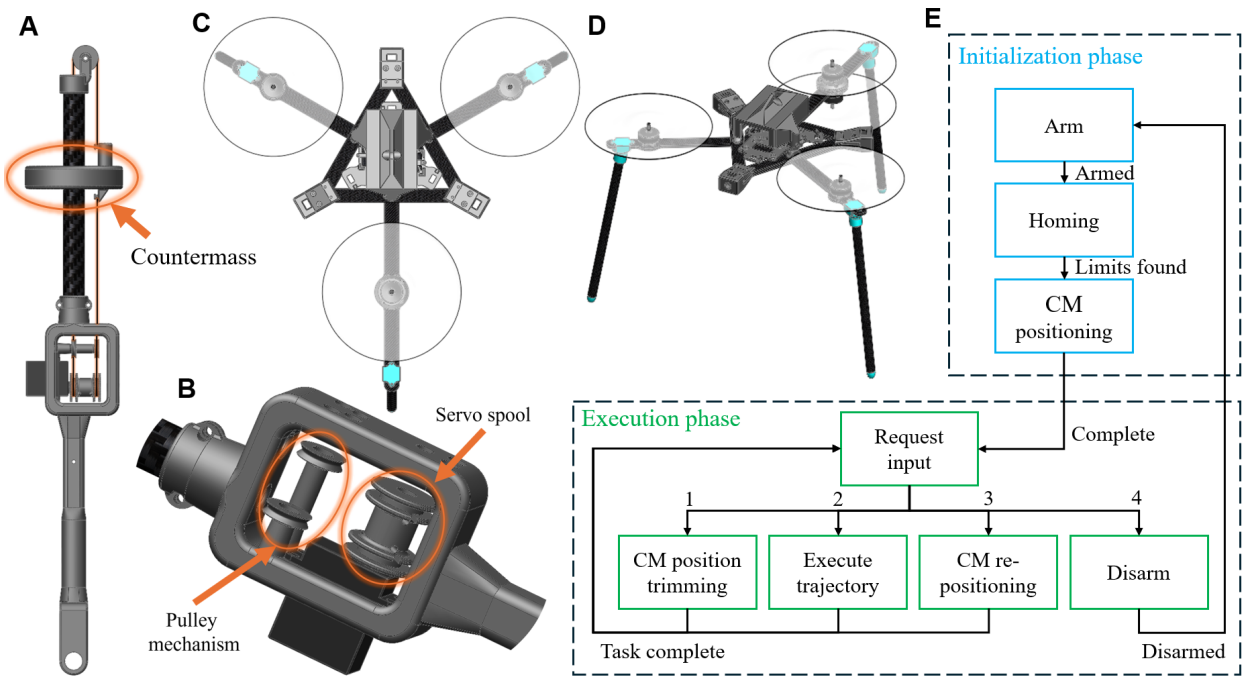

Fig. 4: A) Linear actuator featuring movable countermass. The manipulator can dynamically reconfigure by moving the countermass along the shaft to maintain force-balancing under different payloads. B) Close-up of pulley mechanism driving the linear actuator that moves the countermass. C) Top view of aerial platform without manipulator attached. D) Isometric view. E) FSM diagram showing states and transitions in two phases.

90 g and 150 g. The resulting dimensions were $L_1 = 130$ mm, $L_2 = 310$ mm, $L_3 = 160$ mm, and $m_E = 90$ g

The search algorithm revealed a local optimum for L_1 and L_2, and lighter configurations were found by maximizing L_3 and minimizing the end-effector mass. Thus, the end-effector structure was designed to minimize its mass, yielding a final value of 90.27 g. L_3 was limited to 160 mm to prevent collision of the pantograph's top and aerial platform's body.

With all the dimensions defined, the workspace of the final manipulator was calculated and is shown in Figure 3C.

D. Fast linear actuator design

The countermasses require a fast, lightweight linear actuator to move them into the desired positions, while minimizing reconfiguration time and avoiding excess weight to links L_2 and L_3, which would reduce the countermasses' effectiveness. The actuator's length should be minimized for maximum countermass movement range.

The actuator in Figure 4A and B was developed to meet the design criteria. It uses a servo-driven spool, which pulls a string through pulleys to convert rotational motion into linear movement. The spool has two compartments, each with a string attached. The string in the top compartment passes through a pulley to align with the actuator's cylinder axis, attaching to the bottom of the countermass. The string in the bottom compartment is recentered by another pulley, running through a carbon tube and a pulley at the end of the actuator, before attaching to the top of the countermass. When the servo rotates clockwise, the top string winds onto the spool and the bottom string unwinds, moving the countermass downward (negative $p_{i\text{CM}}$). Counterclockwise rotation moves the countermass upward (positive $p_{i\text{CM}}$).

E. Aerial platform design

A custom aerial platform was designed to fit the manipulator morphology. A trade-off (scores and weights shown in Table I) was used to select from four possible morphologies - tricopter, Y4, quadcopter, and hexacopter. The Y4 morphology was selected for three arm morphology, fitting best with the manipulator's three pantographs. This design also features comparatively low cost and complexity, due to the flight control's similarity with the quadcopter's.

The frame of the aerial platform consists of an equilateral triangle-like shape with the pantographs attached to its vertices. The arms for the motors span from the frame's center through the midpoints of its sides. The front arms span 260 mm whereas the rear arm, with the coaxial motors, spans an extra 75 mm to provide landing gear clearance. The motors are mounted at 200 mm from the center. Top and trimeric views of the custom aerial platform are shown in Figure 4C and D.

TABLE I: Tradeoff table for the selection of the aerial platform configuration.

	Weight	Tricopter	Y4	Quadcopter	Hexacopter
Ease of Integration	5	3	3	1	2
Complexity	3	1	3	3	2
Cost	3	3	2	2	1
Score	NA	27	30	20	19

F. High-level control

A Finite State Machine (FSM), shown in Figure 4E, governs the reconfigurable manipulator through the initialization and execution phases. For trajectory following, joint trajectories are precomputed offline and loaded on the aerial manipulator.

In the initialization phase, the drone waits to be armed by the pilot before homing the countermasses by load feedback on the linear actuators. The countermass are positioned in to balanced configuration. In the execution phase, the FSM asks for user input where different modes can be selected. The experiments are executed in the 'Execute Trajectory' mode.

III. Experiments

Two experiment setups were used: firstly, the system was suspended by ropes to assess the manipulator's force-balancing capabilities; secondly, flight tests evaluate the disturbances from the end-effector movement on the aerial platform's position tracking.

A. Floating base experiments

The aerial manipulator is suspended by cables, allowing the system to swing laterally. Using this setup, the manipulator performs a predefined end-effector trajectory, and the resulting accelerations on the aerial platform are logged for analysis from the Pixracer flight controller's accelerometer. The force-balancing performance of the manipulator is then evaluated by comparing four configurations: unbalanced, balanced, unbalanced with payload, and balanced with payload.

- **Unbalanced:** All countermasses removed.
- **Balanced:** Force-balanced with no payload.
- **Unbalanced with payload:** The same CM positions as the previous configuration ('balanced'), but with a 53 g payload attached to the end-effector.
- **Balanced with payload:** The force-balanced configuration, adjusted for the 53 g payload.

For each configuration, three different end-effector trajectories were performed (in the manipulator base frame): a line trajectory in the x-direction; a line in the y-direction; and a square trajectory on the xy-plane. The line trajectories were performed at $z = 275$ mm and extended from -100 mm to 100 mm. The square trajectory was performed at $z = 300$ mm with (x,y) locations (-100,-100), (100,-100), (100,100), (-100,100) mm. Each trajectory was performed for three end-effector speeds, 0.1 m/s, 0.2 m/s, and 0.4 m/s.

Figure 5 shows the results. The first row of boxplots corresponds to the line trajectory in x-direction, the second row corresponds to the line trajectory along y, and the last row presents the results for the square trajectory on the xy-plane. The first and second columns show the measured and mean corrected accelerations in the x- and y-directions, respectively.

The results reveal that the measured accelerations increase with the end-effector speed. Higher end-effector speed leads to greater accelerations to reach successive end-effector position setpoints, producing larger reaction forces on the manipulator base. This is reflected in the increased interquartile range and the range of whiskers with rising speed for each manipulator configuration, a trend consistent across all trajectories and acceleration components in x and y.

Furthermore, the measured accelerations decrease between the unbalanced configuration and its balanced counterpart, also with payload. Although the accelerations in the balanced configurations are not entirely eliminated, the observed decrease demonstrates the manipulator's force-balancing capabilities. However, when adding a payload to the balanced manipulator configured for no payload, the measured accelerations increase as the manipulator is no longer balanced.

The largest acceleration values for the line trajectories occur in the corresponding movement direction (x or y). For the square trajectory, as expected, the accelerations in the x and y directions are similar.

In addition to being force-balanced, the manipulator must also be statically balanced, where it remains stationary without any external counteracting force from the servos. In a non-balanced configuration, the end-effector drops without servo input, fully extending the pantographs. To verify static balance, the countermasses are moved to their balanced locations, and the end-effector is moved around. The end-effector remains in the last location, confirming static balance. This test was repeated with payload masses, and by reconfiguring the countermass positions the manipulator remains statically balanced with various payload masses.

B. Flight experiments

Similar end-effector trajectory tracking experiments were conducted with the aerial manipulator in flight. The drone hovers at a height of 1 meter. Position estimates from the OptiTrack MoCap system for both the drone and end-effector were collected. The same four manipulator configurations were tested, using only a 35 g payload mass to account for the additional weight of the reflective marker structure needed by the MoCap system, keeping the total end-effector mass equal to the floating base setup.

Two trajectories were performed: a square trajectory on the xy-plane and a line trajectory in the z-direction. The square trajectory was performed at a $z = 350$ mm with (x,y) of (-80,-80), (80,-80), (80,80), and (-80,80) mm. The z-line trajectory ranged from 300 to 400 mm. The results for the square and the z-line trajectory are shown in Figure 6.

Both figures include a plot at the top of the figure with the desired and actual position of the drone and end-effector (showing one repetition for clarity). The box plots below report the absolute position error in x, y, and z.

The square trajectory results demonstrate that force-balanced configurations reduce drone position tracking error in all directions. Notably, the tracking error in z is substantially larger for the unbalanced configuration with payload, showing that the force-balanced configurations reduce disturbances on the aerial platform, improving drone position tracking.

The end-effector tracking error is defined as the drone position error minus the absolute end-effector position, because the drone position errors directly affects the end-effector position. As expected, it is consistent across all configurations and is attributed to kinematic inaccuracy from imperfect fabrication.

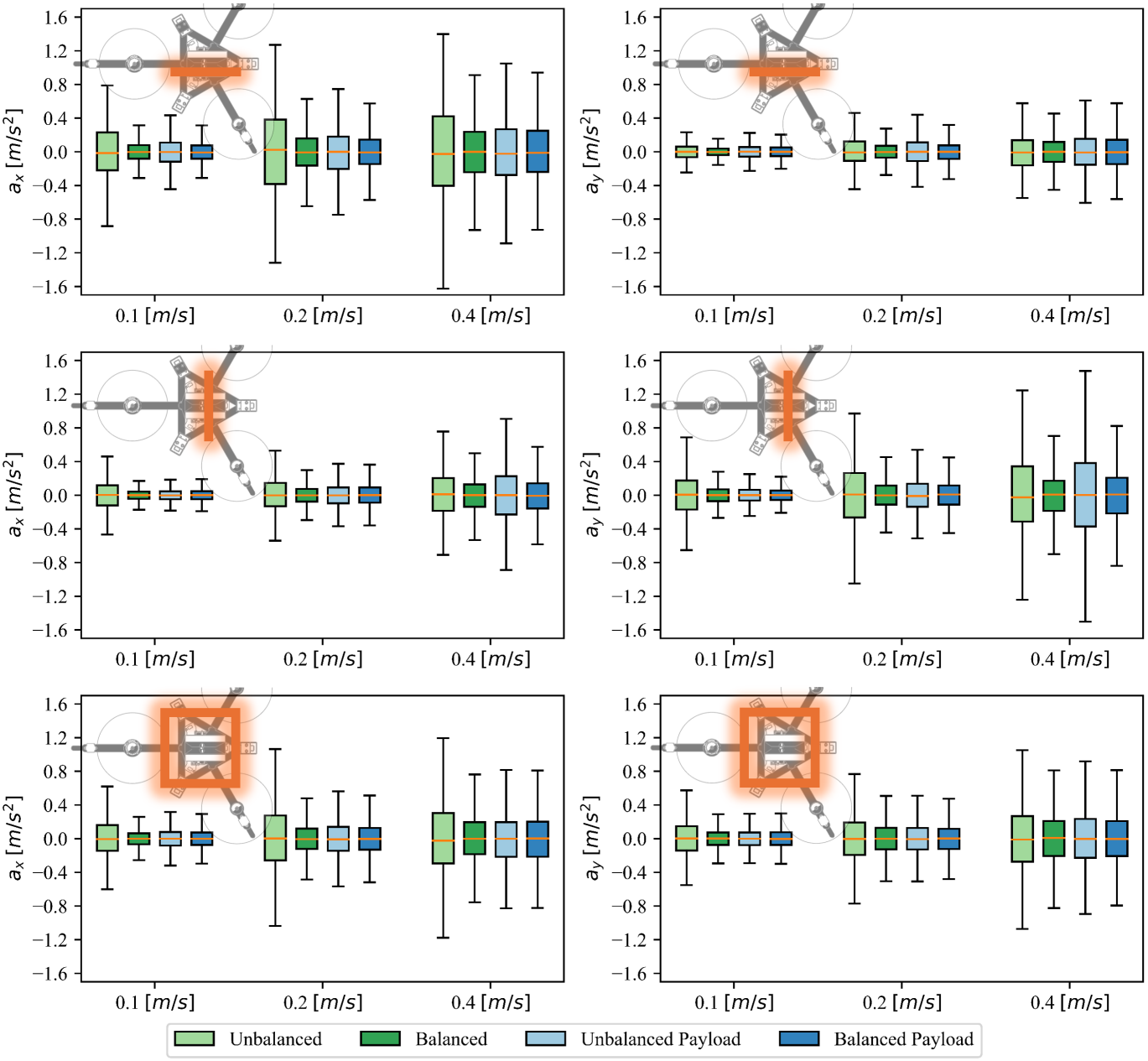

Fig. 5: Floating base test results showing the measured acceleration in x- and y-directions (first and second columns) for line trajectories in x and y (first and second rows), and a square trajectory in the xy-plane (third row). Each trajectory was tested for the four manipulator configurations, and three end-effector speeds (0.1, 0.2, and 0.4 m/s). The measured accelerations generally increase with end-effector speed and the balanced configurations produce lower accelerations than unbalanced ones.

For the z-line trajectory, presented in Figure 6 (right), similar conclusions apply. Drone position errors in z are reduced in the balanced configuration compared to the unbalanced configuration. In x and y, this trend is less consistent; except for the error in x for the unbalanced configuration, the error magnitudes are lower than the error in the z, likely reflecting inherent limitations in the drone's position tracking. The largest difference occurs between the unbalanced and balanced configurations with payload, highlighting the necessity of reconfigurating the manipulator for different payloads.

As with the square trajectory, the end-effector tracking error for the z-line remains consistent across manipulator configurations due to fabrication inaccuracies.

Finally, the mean and standard deviation for the drone's and the end-effector's absolute position errors are summarized in Table II. These statistics are computed over a trajectory set with movement in all axes: a line in the z direction; lines in x- and y-direction; and lastly a square trajectory on the xy-plane. Each trajectory was repeated three times.

The results show that the force-balanced configurations successfully reduce the drone position tracking error. Between the unbalanced and balanced configurations, a 19% decrease

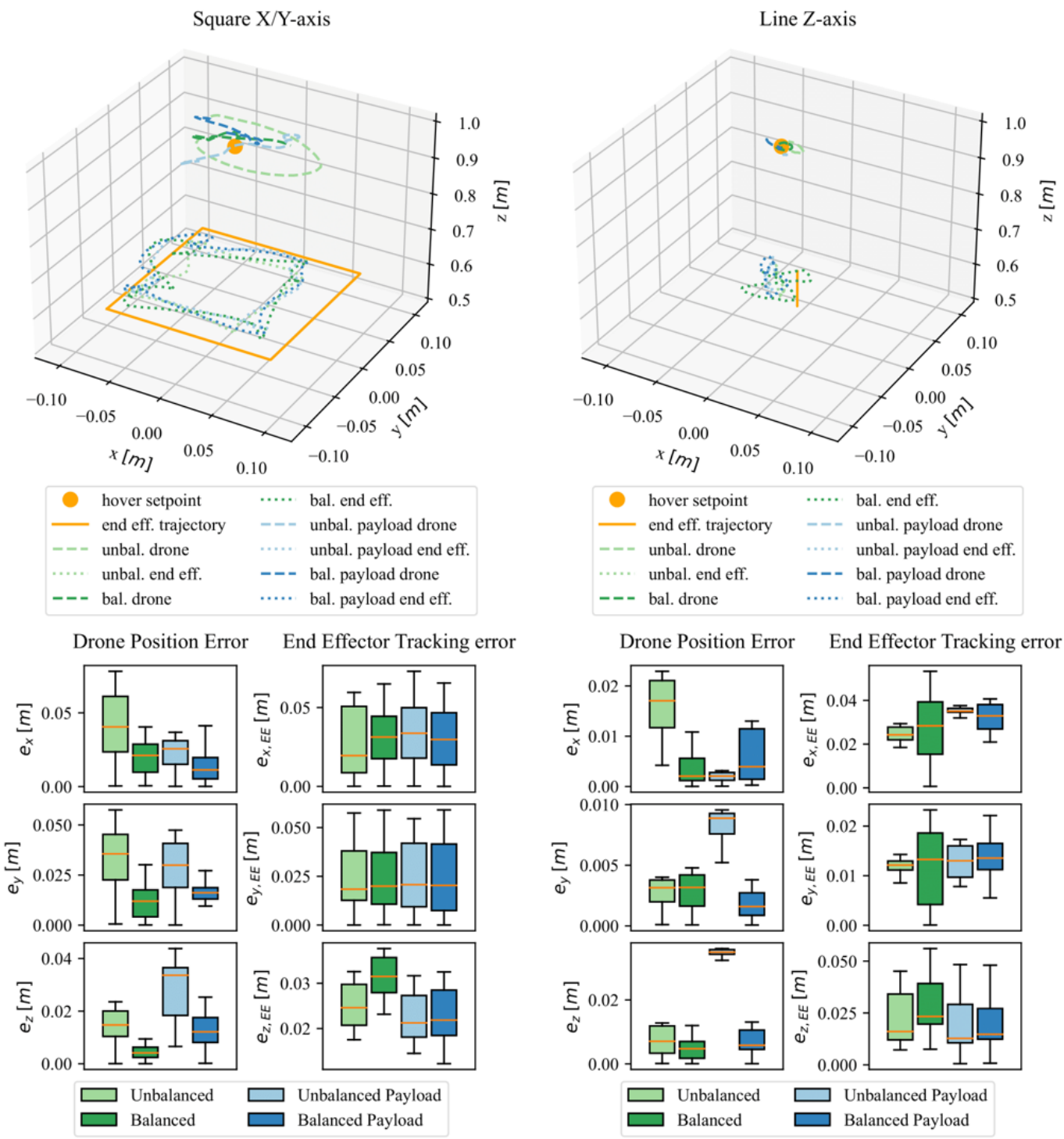

Fig. 6: Position- and box plots for flight tests with square trajectory on the xy-plane and line in z. The four manipulator configurations at 0.1 m/s end-effector speed are shown. The position plots shows a single repetition. The figures show improved drone position tracking with balanced manipulator configurations.

in error was observed with no payload, and a 34% decrease in error was observed with payload. End-effector tracking errors remain consistent across all manipulator configurations, highlighting a systematic error due to imperfect mechanical construction of the manipulator.

IV. Conclusion

This work presents the design, fabrication and testing of a novel aerial manipulator equipped with a reconfigurable force-balanced manipulator. The design of the dynamically reconfigurable force-balanced aerial manipulator, including a custom linear actuator and drone platform, and the fabrication

TABLE II: Mean and standard deviation of the drone and the end-effector position tracking errors. The results show improved drone position tracking for balanced manipulator configurations compared to their unbalanced counterparts.

		Unbalanced	Balanced	Unbalanced payload	Balanced payload
Drone position error	mean [m]	0.043	0.035	0.047	0.031
	std [m]	0.021	0.014	0.015	0.016
End-effector position error	mean [m]	0.047	0.051	0.048	0.049
	std [m]	0.016	0.013	0.015	0.016

of the system were described. Floating base tests demonstrated the manipulator being statically- and force-balanced. Flight tests demonstrated substantial improvement in the drone's position tracking under disturbance from end-effector movements. In conclusion, this work showcased that a smart mechanical design for the manipulator improves the performance of an aerial manipulator and would facilitate the integration of simple controllers, e.g. PID, for dynamic interaction tasks involving varying payloads, e.g. repetitive aerial pick and place.

REFERENCES

[1] Salua Hamaza et al. "Sensor Installation and Retrieval Operations Using an Unmanned Aerial Manipulator". In: *IEEE Robotics and Automation Letters* 4.3 (2019), pp. 2793–2800.

[2] Miguel Ángel Trujillo et al. "Novel Aerial Manipulator for Accurate and Robust Industrial NDT Contact Inspection: A New Tool for the Oil and Gas Inspection Industry". In: *Sensors* 19.6 (2019).

[3] Pisak Chermprayong et al. "An Integrated Delta Manipulator for Aerial Repair: A New Aerial Robotic System". In: *IEEE Robotics & Automation Magazine* 26.1 (2019), pp. 54–66.

[4] Micha Schuster et al. "Automated Aerial Screwing with a Fully Actuated Aerial Manipulator". In: *2022 IEEE/RSJ International Conference on Intelligent Robots and Systems (IROS)*. 2022, pp. 3340–3347.

[5] Alejandro Suárez et al. "Through-Window Home Aerial Delivery System with In-Flight Parcel Load and Handover: Design and Validation in Indoor Scenario". In: *International Journal of Social Robotics* (Oct. 2024), pp. 1–24.

[6] Fabio Ruggiero, Vincenzo Lippiello, and Anibal Ollero. "Aerial Manipulation: A Literature Review". In: *IEEE Robotics and Automation Letters* 3.3 (2018).

[7] Caiwu Ding and Lu Lu. "A Tilting-Rotor Unmanned Aerial Vehicle for Enhanced Aerial Locomotion and Manipulation Capabilities: Design, Control, and Applications". In: *IEEE/ASME Transactions on Mechatronics* 26.4 (2021), pp. 2237–2248.

[8] Carmine Dario Bellicoso et al. "Design, modeling and control of a 5-DoF light-weight robot arm for aerial manipulation". In: *2015 23rd Mediterranean Conference on Control and Automation (MED)*. 2015, pp. 853–858.

[9] Salua Hamaza and Mirko Kovac. "Omni-Drone: on the Design of a Novel Aerial Manipulator with Omnidirectional Workspace". In: *2020 17th International Conference on Ubiquitous Robots (UR)*. 2020.

[10] Volkert van der Wijk and Just Herder. "Dynamic Balancing of Clavel's Delta Robot". In: Jan. 2009, pp. 315–322. ISBN: 978-3-642-01946-3.

[11] Yangnian Wu and C. Gosselin. "Design of reactionless 3-DOF and 6-DOF parallel manipulators using parallelepiped mechanisms". In: *IEEE Transactions on Robotics* 21.5 (2005), pp. 821–833.

[12] Sébastien Briot, Vigen Arakelian, and Sylvain Guégan. "PAMINSA: A new family of partially decoupled parallel manipulators". In: *Mechanism and Machine Theory* 44.2 (2009), pp. 425–444. ISSN: 0094-114X.

[13] Nursultan Imanberdiyev et al. "Design, development and experimental validation of a lightweight dual-arm aerial manipulator with a COG balancing mechanism". In: *Mechatronics* 82 (2022), p. 102719.

[14] Ayham AlAkhras et al. "The Design of a Lightweight Cable Aerial Manipulator with a CoG Compensation Mechanism for Construction Inspection Purposes". In: *Applied Sciences* 12.3 (2022).

[15] Ibrahim Abuzayed et al. "Design of Lightweight Aerial Manipulator with a CoG Compensation Mechanism". In: *2020 Advances in Science and Engineering Technology International Conferences (ASET)*. 2020, pp. 1–5.

[16] Kartik Suryavanshi et al. "ADAPT: A 3 Degrees of Freedom Reconfigurable Force Balanced Parallel Manipulator for Aerial Applications". In: *2023 IEEE International Conference on Robotics and Automation (ICRA)*. 2023, pp. 11936–11942.

[17] Angus B. Clark et al. "On a Balanced Delta Robot for Precise Aerial Manipulation: Implementation, Testing, and Lessons for Future Designs". In: *2022 IEEE/RSJ International Conference on Intelligent Robots and Systems (IROS)*. 2022, pp. 7359–7366.

[18] Jan Jong and Just Herder. "A comparison between five principle strategies for adapting shaking force balance during varying payload". In: Oct. 2015.

[19] Eduardo Castillo Castaneda et al. "Delta robot: Inverse, direct, and intermediate Jacobians". In: *Proceedings of The Institution of Mechanical Engineers Part C-journal of Mechanical Engineering Science - PROC INST MECH ENG C-J MECH E* 220 (Mar. 2006), pp. 103–109.

[20] Yangmin Li. "Kinematic Analysis and Design of a New 3DOF Translational Parallel Manipulator". In: *Journal of Mechanical Design - J MECH DESIGN* 128 (July 2006).

[21] Volkert van der Wijk. "Methodology for analysis and synthesis of inherently force and moment-balanced mechanisms". In: 2014. URL: https://api.semanticscholar.org/CorpusID:108060903.